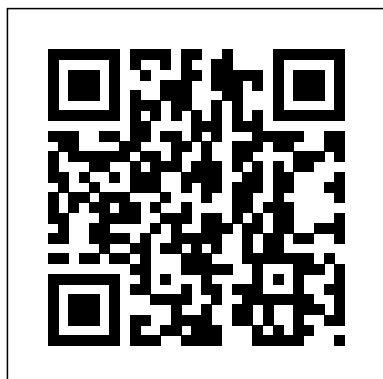


As recognized, adventure as capably as experience approximately lesson, amusement, as skillfully as covenant can be gotten by just checking out a ebook Sb3 after that it is not directly done, you could take even more vis--vis this life, a propos the world.

We allow you this proper as well as easy showing off to get those all. We meet the expense of Sb3 and numerous books collections from fictions to scientific research in any way. accompanied by them is this Sb3 that can be your partner.



Expression of the prolactin gene by lactotropes of the anterior pituitary is modulated by interactions with other lactotropes, with gonadotropes, and with folliculo-stellate cells. However, little is known about which cell-cell adhesion molecules mediate these interactions. We utilized the GH<sub>3</sub> rat anterior pituitary cell line as a model system in which to examine the expression and function of anterior pituitary cell-cell adhesion molecules. Extracellular CaCl<sub>2</sub> induces prolactin mRNA levels by 5-10 fold in GH<sub>3</sub> cells and causes a striking induction of cell-cell adhesion, raising the possibility that the two events are causally linked. Time course experiments indicated the onset of prolactin mRNA always occurred after the onset of cell-cell adhesion and required voltage sensitive calcium channels. Both heparin and trypsin blocked cell-cell adhesion and the prolactin mRNA induction without affecting the levels of other mRNAs. Based on these data we propose a role for both voltage-sensitive calcium channels and calcium-dependent cell-cell adhesion in the CaCl<sub>2</sub> induction of prolactin gene expression. Cadherins may mediate GH<sub>3</sub> cell-cell adhesion based on the observation of adherens junctions between GH<sub>3</sub> cells. Experiments were inconclusive which used cadherin-specific blocking agents such as N-cadherin antisense oligonucleotides and an N-cadherin blocking antibody in attempts to block the calcium-dependent induction of cell-cell adhesion and prolactin mRNA. This raised the possibility that multiple cadherins and/or other cell-cell adhesion molecules were expressed in GH<sub>3</sub> cells and contributed to calcium-dependent cell-cell adhesion as well. Studies supporting this hypothesis indicated that N-cadherin, R-cadherin, and cadherin-9 were expressed in GH<sub>3</sub> cells. All three mRNAs were induced by cycloheximide, indicating that they may be regulated at the level of mRNA stability. N-cadherin transcripts were detected in male and cycling female adult rat anterior pituitaries, but were downregulated in anterior pituitaries from pregnant rats. These studies raise the possibility that cell-cell adhesion and cadherin expression plays a functional role

in the regulation of the lactotrope phenotype. The findings reported in this book on the methods of cluster measurements will lead to new avenues using nondestructive mass spectrometry and dipole mass isomers. Much attention is given to the physics and chemistry of fullerenes and nanotubes, including the problems surrounding the formation and growth of nanotubes, electron characteristics of fullerenes, the influence of solvents, simulation of the properties of carbon clusters, etc. Some unique experimental data on the conversion of aerosols into aerogels with the formation of fractal structures is provided. In addition, the book covers one of the most interesting subjects of modern physics -- fractal clusters.

The photochemical reaction of Mn<sub>2</sub>(CO)<sub>10</sub> with HSnBu<sub>3</sub> has been studied by continuous photolysis. Sunlamp irradiation of a CO-saturated hexane solution of Mn<sub>2</sub>(CO)<sub>10</sub> and HSnBu<sub>3</sub> results in formation of HMn(CO)<sub>5</sub> and Bu<sub>3</sub>SnMn(CO)<sub>5</sub> in equimolar quantities. The rate of disappearance of Mn<sub>2</sub>(CO)<sub>10</sub> and formation of products exhibit an inverse (CO) dependence. When the reaction of Mn<sub>2</sub>(CO)<sub>10</sub> with HSnBu<sub>3</sub> is performed under 1 atm AR, the rate of disappearance of Mn<sub>2</sub>(CO)<sub>10</sub> is much faster than when CO is present, HMn(CO)<sub>5</sub> forms in much greater quantities than Bu<sub>3</sub>SnMn(CO)<sub>5</sub>, and a third product, identified as HMn(CO)<sub>4</sub>(SnBu<sub>3</sub>)<sub>2</sub>, forms as the other major product. The above observations are consistent with a mechanism involving oxidative addition of HSnBu<sub>3</sub> to Mn<sub>2</sub>(CO)<sub>9</sub>. The reactions of HSnBu<sub>3</sub> with Mn(CO)<sub>4</sub>L<sub>2</sub> (L = CO or PR<sub>3</sub>) and Mn<sub>2</sub>(CO)<sub>7</sub>L<sub>2</sub> were studied by flash photolysis. In every case examined, HSnBu<sub>3</sub> undergoes oxidative addition with Mn<sub>2</sub>(CO)<sub>7</sub>L<sub>2</sub>. However, H-atom transfer to Mn(CO)<sub>4</sub>L<sub>2</sub> does not occur. For L = CO, PMe<sub>3</sub>, P(i-Bu)<sub>3</sub>, and P(O-i-Pr)<sub>3</sub>, the initial product of oxidative addition, Mn<sub>2</sub>(CO)<sub>7</sub>L<sub>2</sub>(H)(SnBu<sub>3</sub>), is observed. At longer time intervals, this intermediate disappears by reductive elimination of HMn(CO)<sub>4</sub>L. Mn<sub>2</sub>(CO)<sub>7</sub>L<sub>2</sub>(H)(SnBu<sub>3</sub>) is not observed when the metal center is crowded as in the cases of L = P(i-Pr)<sub>3</sub> and P(C<sub>6</sub>H<sub>11</sub>)<sub>3</sub> because oxidative addition is slow relative to reductive elimination. The transient absorbance decay of Mn<sub>2</sub>(CO)<sub>7</sub>L<sub>2</sub> in the presence of

$\text{HSnBu}\text{\sb3}$  obeys pseudo-first-order kinetics. Plots of  $K\text{\sb{\rm obs}}$  vs.  $(\text{HSnBu}\text{\sb3})$  are linear for  $L = P(i\text{-Bu})\text{\sb3}$ ,  $P(i\text{-Pr})\text{\sb3}$ , and  $P(C\text{\sb6}H\text{\sb{11}})\text{\sb3}$ . However, for  $L = P\text{Me}\text{\sb3}$  and  $P(n\text{-Bu})\text{\sb3}$ , the  $k\text{\sb{\rm obs}}$  vs  $(\text{HSnBu}\text{\sb3})$  plot is non-linear throughout the entire  $(\text{HSnBu}\text{\sb3})$  range. A mechanism involving a rate determining equilibrium between unbridged  $\text{Mn}\text{\sb2}(\text{CO})\text{\sb7}L\text{\sb2}$  and semi-bridged  $\text{Mn}\text{\sb2}(\text{CO})\text{\sb7}L\text{\sb2}$  prior to oxidative addition of  $\text{HSnBu}\text{\sb3}$  accounts for the experimental observations.

#### Structure-Performance Relationships in Surfactants

Environmental Effects on the Rate of Intramolecular Electron Transfer in Trinuclear Mixed-valence Transition Metal Carboxylate Complexes in the Solid State

New York City Charter and Administrative Code, Annotated

The Dictionary of Practical Phonography, Giving the Best Phonographic Forms for the Words of the English Language (sixty Thousand), and for Over Five Thousand Proper Names; Also Illustrating the Principles of Phrase-writing

Zeitschrift Für Naturforschung  
Organometallic Imido, Sulfido and Oxo Complexes of Osmium (vi)

#### SB3: Green

The tetraphenylphosphonium, bis(triphenylphosphoranylidene)ammonium, and n-butylammonium salts of tetrachlorodioxosmium were prepared. Alkylation of  $(\text{PPh}\text{\sb4}) (\text{Os}(\text{O})\text{\sb2}\text{Cl}\text{\sb4})$  with trimethylsilylmethylmagnesium chloride yields oxotetrakis(trimethylsilylmethyl)osmium. The crystal structure of  $\text{Os}(\text{O})(\text{CH}\text{\sb2}\text{SiMe}\text{\sb3})\text{\sb4}$  was determined. The physical properties and reaction chemistry of isoelectronic alkyl complexes of osmium(VI), n-butylammonium nitridotetrakis-(trimethylsilylmethyl)osmium, methylimidotetrakis(trimethylsilylmethyl)osmium, and  $\text{Os}(\text{O})(\text{CH}\text{\sb2}\text{SiMe}\text{\sb3})\text{\sb4}$  are compared. The nitrido complex does not react with carbon monoxide while both the methyl imide and oxo compounds are reductively carbonylated under CO pressure. The methylimido complex reacts to produce the acyl derivatives,  $\text{Os}(\text{N})(\text{C}(\text{O})\text{CH}\text{\sb2}\text{SiMe}\text{\sb3})(\text{CH}\text{\sb2}\text{SiMe}\text{\sb3})\text{\sb3}$  and  $\text{Os}(\text{N})(\text{C}(\text{O})\text{CH}\text{\sb2}\text{SiMe}\text{\sb3})\text{\sb2}(\text{CH}\text{\sb2}\text{SiMe}\text{\sb3})\text{\sb2}$ . A mono insertion product is produced in reaction of the methylimide with tert-butylisocyanide. The nitrido complex forms Lewis acid adducts, is alkylated by organic electrophiles, and reacts with mineral acids. Electrophilic cleavage is slower in the methylimido complex while the oxo complex is stable towards electrophiles. The observed differences in reactivity can be ascribed to subtle changes in bonding between the metal and the terminal heteroatom ligand, and to the formation of a structural isomer of the methylimido complex. Pentahaptocyclopentadienylnitridobis(trimethylsilylmethyl)osmium and pentamethylcyclopentadienylnitridobis(trimethylsilylmethyl)osmium can be made from sodium cyclopentadienide or lithium pentamethylcyclopentadienide and n-butylammonium dichlorobis(trimethylsilylmethyl)osmium. The addition of silver tetrafluoroborate to  $(\text{Etasp5-C}\text{\sb5}H\text{\sb5})\text{Os}(\text{N})(\text{CH}\text{\sb2}\text{SiMe}\text{\sb3})\text{\sb2}$  formed a silver dimer,  $\text{Os}(\text{N})(\text{CH}\text{\sb2}\text{SiMe}\text{\sb3})\text{\sb2}\text{Ag}(\text{BF}\text{\sb4})$ . The compound reacted with boron trifluoride to form an adduct in solution and with methyltrifluoromethane sulfonate to form the

methylimide,  $(\text{Etasp5-C}\text{\sb5}H\text{\sb5})\text{Os}(\text{NMe})(\text{CH}\text{\sb2}\text{SiMe}\text{\sb3})\text{\sb2}$  (OSO $\text{\sb2}$ CF $\text{\sb3}$ ). The crystal structure of the silver dimer was determined. The phosphine complex,  $\text{Os}(\text{N})\text{Cl}(\text{CH}\text{\sb2}\text{SiMe}\text{\sb3})\text{\sb2}(\text{PMe}\text{\sb3})\text{\sb2}$ , was prepared from  $(\text{N-n-Bu}\text{\sb4})$

$(\text{Os}(\text{N})\text{Cl}\text{\sb2}(\text{CH}\text{\sb2}\text{SiMe}\text{\sb3})\text{\sb2})$  and  $\text{PMe}\text{\sb3}$ . The salt,  $(\text{Os}(\text{N})(\text{CH}\text{\sb2}\text{SiMe}\text{\sb3})\text{\sb2}(\text{PMe}\text{\sb3})\text{\sb2})(\text{BF}\text{\sb4})$ , was prepared by addition of  $\text{AgBF}\text{\sb4}$  to the chloride compound. NMR and conductivity studies determined that the chloride compound was neutral while the  $\text{BF}\text{\sb4}$  product was cationic. The addition of n-butyl lithium to  $\text{Os}(\text{N})\text{Cl}(\text{CH}\text{\sb2}\text{SiMe}\text{\sb3})\text{\sb2}(\text{PMe}\text{\sb3})\text{\sb2}$  formed n-butylnitrido-bis(trimethylsilylmethyl)osmium.

Synthesis of Finite State Machines: Logic Optimization is the second in a set of two monographs devoted to the synthesis of Finite State Machines (FSMs). The first volume, Synthesis of Finite State Machines: Functional Optimization, addresses functional optimization, whereas this one addresses logic optimization. The result of functional optimization is a symbolic description of an FSM which represents a sequential function chosen from a collection of permissible candidates. Logic optimization is the body of techniques for converting a symbolic description of an FSM into a hardware implementation. The mapping of a given symbolic representation into a two-valued logic implementation is called state encoding (or state assignment) and it impacts heavily area, speed, testability and power consumption of the realized circuit. The first part of the book introduces the relevant background, presents results previously scattered in the literature on the computational complexity of encoding problems, and surveys in depth old and new approaches to encoding in logic synthesis. The second part of the book presents two main results about symbolic minimization; a new procedure to find minimal two-level symbolic covers, under face, dominance and disjunctive constraints, and a unified frame to check encodability of encoding constraints and find codes of minimum length that satisfy them. The third part of the book introduces generalized prime implicants (GPIs), which are the counterpart, in symbolic minimization of two-level logic, to prime implicants in two-valued two-level minimization. GPIs enable the design of an exact procedure for two-level symbolic minimization, based on a covering step which is complicated by the need to guarantee encodability of the final cover. A new efficient algorithm to verify encodability of a selected cover is presented. If a cover is not encodable, it is shown how to augment it minimally until an encodable superset of GPIs is determined. To handle encodability the authors have extended the frame to satisfy encoding constraints presented in the second part. The covering problems generated in the minimization of GPIs tend to be very large. Recently large covering problems have been attacked successfully by representing the covering table with binary decision diagrams (BDD). In the fourth part of the book the authors introduce such techniques and extend them to the case of the implicit minimization of GPIs, where the encodability and augmentation steps are also performed implicitly. Synthesis of Finite State Machines: Logic Optimization will be of interest to researchers and professional engineers who work in the area of computer-aided design of integrated circuits.

The Dictionary of Practical Phonography  
Novel PET Radiotracers with Potential Clinical Applications, An Issue of PET Clinics, E-Book  
Special Report - Highway Research Board  
JJAP  
Competing Reaction Pathways in the Photochemical Reactions of Metal Carbonyl Compounds  
SB3: St. Brittany's Checkmate  
Tridentate triply bridging phosphonate and arsonate clusters of the general formula  $(\mu\text{-H})\text{\sb2}\text{Os}\text{\sb3}(\text{CO})\text{\sb9}(\mu\text{\sb3})$ ,

$\eta\text{-Os}(\text{CO})_2(\text{P}(\text{R})\text{OEt})_2$  (E = P, R = Ph (1), Me; E = As, R = Ph) were prepared. The reaction scheme involved (1) generation of a solution containing a labile cluster species by reaction of  $\text{Os}(\text{CO})_2(\text{CH}_3)_2$  with neat trifluoromethanesulfonic (triflic) acid, (2) addition of a large excess of the appropriate free acid, and (3) water quench. A diffraction study of 1 showed the capping  $\text{PhPO}(\text{O})_2$  ligand in a triply bridging tridentate coordination mode. Compound 1 is fluxional, and hydride migration was established as the low barrier dynamic process. Solid/solution structure equivalence for this class of clusters was demonstrated. The bis triflate cluster  $\text{Os}_2(\text{CO})_8(\text{O}(\text{SCF}_3))_2$  was isolated (76% yield) from the triflic acid/ $\text{Os}(\text{CO})_2(\text{CH}_3)_2$  solution. It reacts with neat carboxylic acids to give clusters of the general formula  $(\mu\text{-H})\text{Os}_2(\text{CO})_8(\mu\text{-H})$ ,  $\eta\text{-Os}_2(\text{CO})_8(\eta\text{-O}(\text{SCF}_3))$  (R = H,  $\text{CF}_3$ ) and  $(\mu\text{-H})\text{Os}_2(\text{CO})_8(\mu\text{-H})$ ,  $\eta\text{-Os}_2(\text{CO})_8(\eta\text{-O}(\text{SCF}_3))$  (R = H,  $\text{CH}_3$ ,  $\text{CF}_3$ ). A diffraction study of  $(\mu\text{-H})\text{Os}_2(\text{CO})_8(\mu\text{-H})$ ,  $\eta\text{-Os}_2(\text{CO})_8(\eta\text{-O}(\text{SCF}_3))$  showed the oxyligands in the trans axial configuration. This compound was found to be unreactive towards a variety of potential ligands (e.g. THF,  $\text{NCCF}_3$ , CO). It did react with halides and thiosulfate to give  $\text{HOs}(\text{CO})_2\text{X}$  derivatives and  $\text{Os}(\text{CO})_2(\mu\text{-S})$  respectively. Reaction of  $\text{Os}_2(\text{CO})_8(\text{O}(\text{SCF}_3))_2$  with acetonitrile gave  $(\mu\text{-H})\text{Os}_2(\text{CO})_8(\text{NCCF}_3)_2$  ( $\text{O}(\text{SCF}_3))_2$ . This cluster exists as isomers at low temperature ( $-30^\circ\text{C}$ ). These isomers interconvert by hydride migration.  $\text{Os}(\text{CO})_{12}$  chemisorbed to silica has been examined by magic-angle-spinning  $^{13}\text{C}$  NMR, and the structure of the chemisorbed species identified as  $(\mu\text{-H})\text{Os}_3(\text{CO})_9(\mu\text{-OSi=})$  by comparison with model compounds. Molecular models, such as  $(\mu\text{-H})\text{Os}_3(\text{CO})_{11}(\eta\text{-O}(\text{SCF}_3))$ , for possible intermediates in the chemisorption reaction were prepared.

The Defense Waste Processing Facility (DWPF) is presently vitrifying Sludge Batch 3 (SB3) and preparing to process Sludge Batch 4 (SB4) in late 2006 or early 2007. Previous laboratory testing and DWPF operational experience has indicated that the maximum waste throughput peak for the Sludge Batch 2 (SB2) system occurs at a waste loading in the mid-30's. This trend has been shown as well for SB3 on a lab-scale basis. These SB3 tests used SRAT product that targeted a REDuction/OXidation (REDOX) of 0.2 and an acid stoichiometry of 135%. Acid stoichiometry, however, has been shown to impact melt rate of MRF tests at one waste loading (35%). Due to the impact of acid stoichiometry on melt rate, it is possible that the current target acid stoichiometry (155%) with SB3 may not exhibit the same maximum waste throughput peak, or there may not even be a discernable peak. In fact, current DWPF operational experience with SB3 and Frit 418 has not shown the same drop off in melt rate and hence waste throughput as was observed with SB2 and Frit 320. The objective of this testing is to determine if increasing the overall alkali content in the feed (via using the higher alkali Frit 320 versus Frit 418) will either result in a shift in the waste throughput to higher waste loadings or an increase in the overall waste throughput at waste loadings of interest (31 to 41%). For these tests, the target Sludge Receipt and Adjustment Tank (SRAT) product REDOX was 0.2 and the target acid stoichiometry was 155%. The incentive for this series of tests stems from a previous Slurry-Fed Melt Rate Furnace (SMRF) test with SB3/Frit 320 feed which showed an increase in melt rate versus SB3/Frit 418 at 35% waste loading. This single data point suggests that overall waste throughput for the SB3/Frit 320 system is higher at 35% waste loading (i.e., the melt rate versus waste loading curve has potentially shifted upward). To address the potential shift in waste throughput, the strategy was to fully characterize the impact of waste loading (ranging from about 30 to 40%) on melt rate for the SB3/Frit 320 and SB3/Frit 418 feed systems. This will allow for potential shifts in waste throughput to be assessed via a change in frit composition. Initially, the dry-fed Melt Rate Furnace (MRF) was utilized. Based on the MRF results, the tests had a decision point on whether or not to continue testing using the SMRF.

[Volume 1] contains the New York City Charter; [volumes 2]-[22] contain the Administrative Code.  
Bituminous Mixtures and Pavements VII  
Final

Seeking the American Revolution SB3 Forward, March!

Gold(I) Oxo, Imido, Hydrazido Complexes and Gold Clusters

Toxic interactions of metal ions ( $\text{Cd}^{2+}$ ,  $\text{Pb}^{2+}$ ,  $\text{Zn}^{2+}$  and  $\text{Sb}^{3-}$ ) on in vitro biomass production of ectomycorrhizal fungi

The Chemistry of Cyclopentadienyl Ruthenium Complexes Containing Thiolato Or Catenated Polysulfano Ligands

Key Revolutionary War battles and their significance are recounted along with a glimpse of how the battles are reenacted today.

In response to intensifying interest on surfactant research brought on by recent innovation, Structure-Performance Relationships in Surfactants, Second Edition examines novel developments in our understanding of the properties and performance of surfactants at air-liquid, liquid-liquid, and solid-liquid interfaces, highlighting seven new chapters and carefully updated material to reflect current trends. This edition presents new material on the adsorption of vesicle-forming surfactants at the air-water interface, fluorinated surfactants having two hydrophobic chains, surface-active properties of telomer-type surfactants having several hydrocarbon chains, and the association behavior of amphiphilic dendritic polymers, among many other topics.

The Michigan Basin is a classic intracratonic basin that has played a significant role in the fundamental understanding of geological processes in such basins, and has been an important resource for oil and gas, economic minerals, groundwater, and coal. Despite the classic nature of the Michigan Basin, there has not been a "special volume" dedicated to the basin in nearly 25 years. Since that time, new advancements in the geological sciences, particularly the utilization of high-resolution sequence stratigraphy and three-dimensional geostatistical modeling, have led to a new and more comprehensive understanding of the Paleozoic sedimentary packages of the Michigan Basin. This volume provides significant new insights of the Michigan Basin to both academic and applied geoscientists; it includes papers that discuss various aspects of the sedimentology and stratigraphy of key units within the basin, as well as papers that analyze the diverse distribution of natural resources present in this basin.

American Chess Bulletin

Vibrational Predissociation Spectroscopy of Hydrogen Bonded Complexes in the 10 Micron Region

Initial report

Maximizing SB3 Waste Throughput Melt Rate Tests

Cell-cell Adhesion and Cadherin Expression in the  $\text{Gh}(\text{Sb}^3)$  Somatotropin Cell Line: Implications for Prolactin Gene Expression

Oxo, Imido, and Nitrido Compounds of Osmium(VI)

Frank and Brittany are back! Life has started to settle in again after their last adventure. Brittany is still pregnant with their second child, and they both are enjoying their jobs, but they are concerned about the future. Like most young couples with children, Brittany wants to spend more time at home. But health insurance and income cuts, and looming decisions about their apartment house converting to condos seem to conspire against this. Brittany has also begun to worry about Frank; his attitude has become flippant and cocky. He doesn't seem to be taking his responsibilities seriously. And he hasn't--until a tragic accident finally gets his attention. And then all hell breaks loose.

The science and technology in the area of piezoelectric ceramics are extremely progressing, especially the materials research, measurement technique, theory and applications, and furthermore, demanded to fit social technical requests such as environmental problems. While they had been concentrated on piezoelectric ceramics composed of lead-containing compositions, such as lead zirconate titanate (PZT) and lead titanate, at the beginning because of the high piezoelectricity,

recently lead water pollution by soluble PZT of our environment must be considered. Therefore, different new compositions of lead-free ceramics in order to replace PZT are needed. Until now, there have been many studies on lead-free ceramics looking for new morphotropic phase boundaries, ceramic microstructure control to realize high ceramic density, including composites and texture developments, and applications to new evaluation techniques to search for high piezoelectricity. The purpose of this book is focused on the latest reports in piezoelectric materials such as lead-free ceramics, single crystals, and thin films from viewpoints of piezoelectric materials, piezoelectric science, and piezoelectric applications. Vibrational predissociation spectroscopy of isotopomers of  $(\text{CH}_3\text{OH})_2$  and  $\text{Ar}(\text{CH}_3\text{OH})$  were recorded in the 10 micron region, where the C-O stretching transition is located. Using the beam depletion technique, spectra were recorded for  $(\text{CH}_3\text{OH})_2$ ,  $(\text{CH}_3\text{OD})_2$ ,  $(\text{CD}_3\text{OD})_2$ ,  $(\text{CH}_3\text{OH})(\text{CH}_3\text{OD})$ ,  $(\text{CH}_3\text{OD})(\text{CD}_3\text{OD})$ ,  $(\text{CH}_3\text{OX})\text{Ar}$  ( $X = \text{H}, \text{D}$ ) and  $(\text{CD}_3\text{OD})\text{Ar}$ . It is observed that in the mixed dimers, complexes, the measured C-O transition frequencies are unchanged from their respective monomers. Time of flight measurements were also conducted to determine the translational temperature of the complexes. A band contour analysis was done to estimate the homogeneous and inhomogeneous contribution to the observed linewidths. All of the complexes except the ones containing  $\text{CH}_3\text{OD}$  methanol had a homogeneous contribution of no greater than  $1 \text{ cm}^{-1}$ . The complexes involving  $\text{CH}_3\text{OD}$  have a homogeneous width of less than  $0.5 \text{ cm}^{-1}$ . A transition dipole coupling model was studied to reveal that only  $1 \text{ cm}^{-1}$  out of the  $25 \text{ cm}^{-1}$  of splitting observed in  $(\text{CH}_3\text{OH})_2$  is due to dipole-dipole interactions. The model does not predict the isotopic shift in  $(\text{CH}_3\text{OH})(\text{CH}_3\text{OD})$  for either the donor or acceptor C-O stretching transition. Integral dissociation cross sections were also measured for the different species, with good agreement with a previous measurement by another group for  $(\text{CH}_3\text{OH})_2$ . The measured integral dissociation cross sections for the various deuterated dimers decreased with the number of deuterium atoms within the complex. Preliminary studies of  $(\text{CH}_3\text{NH}_2)_2$ ,  $\text{Ar}(\text{CH}_3\text{NH}_2)$ ,  $(\text{CH}_3\text{CH}_2\text{OH})_2$ ,  $\text{Ar}(\text{CH}_3\text{CH}_2\text{OH})$ ,  $((\text{CH}_3)_3\text{COH})_2$ ,  $\text{Ar}(1,4\text{-dioxane})$ ,  $(1,4\text{-dioxane})_2$ ,  $\text{Ar}(d_6\text{-acetone})$  and  $(d_6\text{-acetone})_2$  were also carried out in the 10 micron region.

Progress in the Physics of Clusters

Oxyligands in Triosmium Carbonyl Cluster Compounds

SB3: Green

Inorganic Ion Exchangers in Chemical Analysis

Paleozoic Stratigraphy and Resources of the Michigan Basin

15th International Conference, RSFDGrC 2015, Tianjin, China, November 20-23, 2015, Proceedings

Highway engineers are facing the challenge not only to design and construct sustainable and safe pavements properly and economically. This implies a thorough understanding of materials behaviour, their appropriate use in the continuously changing environment, and implementation of constantly improved technologies and methodologies. Bituminous Mixtures and Pavements VII contains more than 100 contributions that were presented at the 7th International Conference ' Bituminous Mixtures and Pavements ' (7ICONFBMP, Thessaloniki, Greece 12-14 June 2019). The papers cover a wide range of topics: - Bituminous binders - Aggregates, unbound layers and subgrade - Bituminous mixtures (Hot, Warm and Cold) - Pavements (Design, Construction, Maintenance, Sustainability, Energy and environment consideration) - Pavement management - Pavement recycling - Geosynthetics - Pavement assessment, surface characteristics and safety - Posters Bituminous Mixtures and Pavements VII reflects recent advances in

highway materials technology and pavement engineering, and will be of interest to academics and professionals interested or involved in these areas.

This book constitutes the refereed conference proceedings of the 15th International Conference on Rough Sets, Fuzzy Sets, Data Mining and Granular Computing, RSFDGrC 2015, held in Tianjin, China in November 2015 as one of the co-located conference of the 2015 Joint Rough Set Symposium, JRS 2015. The 44 papers were carefully reviewed and selected from 97 submissions. The papers in this volume cover topics such as rough sets: the experts speak; generalized rough sets; rough sets and graphs; rough and fuzzy hybridization; granular computing; data mining and machine learning; three-way decisions; IJCRS 2015 data challenge.

This issue of PET Clinics focuses on Radiotracers, and is edited by Drs. Neil Vasdev and Abass Alavi. Articles will include: PET/CT detection of HER2-positive metastases in patients with 89Zr-DFO-trastuzumab; uPAR-PET with 68Ga-NOTA-AE105: first clinical experience with a novel PET ligand; 64Cu-FBP8: A fibrin-targeted probe for imaging of thrombus; Imaging of synaptic density in the brain via synaptic vesicle glycoprotein 2A (SV2A) with a novel biomarker [11C]UCB-J; Neuroimaging of stress sensitive and neuroinflammatory targets in mood disorders; Impact of MR-based PET motion correction on the quantification of PET kinetic parameters in simultaneous cardiac PET-MR; Multimodal studies of the contributions of amyloid and tau burden to neurodegeneration in AD, FTD and Non-AD tauopathies; Imaging of prostate-specific membrane antigen (PSMA) using [18F]DCFPyL; Ga-68 GRPR antagonist imaging; and more!

Ferromagnetism in the Kondo lattice  $\text{CeNiSb}_3$  and  $\text{CeZn}_x\text{Sb}_2$  ( $x$

A Complete Text of the New York City Charter and the New York City Administrative Code with Court Decisions from the Time of the Enactment of the Code and Charter  
Proceedings of the Ocean Drilling Program

The Synthesis and Stereodynamics of Cyclopentadienyl Ruthenium Chalcogenide Clusters

Post-fire Treatment Effectiveness for Hillslope Stabilization  
Rough Sets, Fuzzy Sets, Data Mining, and Granular Computing

In a series of the isostructural ( $R32$  space group) mixed-valence  $(\text{Fe}_3\text{O}(\text{O}_2\text{CCH}_3)_6(4\text{-Me-Py})_3) \cdot S$  complexes, where (4-Me-Py) is 4-methylpyridine and S is a solvate molecule, we have found that systematic changes of solvate molecules have a pronounced impact on the phase transitions at which a given complex valence detrap. This sensitivity is a reflection of the fact that the lowest energy electronic states of  $\text{Fe}_3\text{O}$  complexes are vibronic and as a result these complexes are very sensitive to their environment. It is also found that the  $\text{CHCl}_3$  solvate complex exhibits a very abrupt phase transition at low temperature (95K) and the  $\text{CH}_3\text{CCl}_3$  solvate complex exhibits a phase transition at 125K.  $^{57}\text{Fe}$  Mossbauer spectra of this  $\text{CHCl}_3$  solvate complex show that this complex valence-detrap at  $\sim 95\text{K}$ . However, the complex with the less symmetric  $\text{CH}_3\text{CHCl}_2$  solvate molecule becomes valence-detraped at  $\sim 45$  degrees higher than for the  $\text{CH}_3\text{CCl}_3$  complex and  $\sim 75$  degrees higher than for the  $\text{CHCl}_3$  complex. Changing the solvate molecules may lead to changes in the intermolecular interactions propagated via the pyridine-pyridine overlaps between neighboring  $\text{Fe}_3\text{O}$  molecules. The introduction of the bulky solvate ( $\text{CH}_3\text{CCl}_3$ ) and less

symmetric solvate ( $\text{CH}_3\text{CHCl}_2$ ) gives rise to less intermolecular interactions between neighboring  $\text{Fe}_3\text{O}$  molecules and, consequently, gives higher transition temperature than that of the  $\text{C}_3$  symmetry  $\text{CHCl}_3$  solvate. In fact, the results of CNDO/2 molecular orbital calculations show that an important factor is the intermolecular interactions between the 4-Me-Py $\cdots$ 4-Me-Py ligands for controlling the intramolecular electron transfer rate in addition to the onset of solvate molecules dynamic motion. Interestingly, solid-state  $^1\text{H}$  NMR studies of  $(\text{Fe}_3\text{O}(\text{O}_2\text{CCH}_3)_6(\text{Py})_3)$  ( $\text{CDCl}_3$ ) and  $(\text{Fe}_3\text{O}(\text{O}_2\text{CCH}_3)_6(4\text{-Me-Py})_3)$  ( $\text{CDCl}_3$ ) show that the  $\text{C}_3$ -symmetry  $\text{CHCl}_3$  molecule synchronously moves with the changes of the vibronic coordinates in neighboring  $\text{Fe}_3\text{O}$  molecules in the lattice. Thus, we can suggest that another important factor in controlling the rate of electron transfer may be the van der Waals interactions between a solvate molecule and neighboring  $\text{Fe}_3\text{O}$  complexes. This van der Waals interactions may be large enough to modify the ground state potential-energy surface for a  $\text{Fe}_3\text{O}$  complex to affect the rate at which such a complex can tunnel from one vibronic minimum to another. Finally, we have discovered the first trinuclear iron acetate complex  $(\text{Fe}_3\text{O}(\text{O}_2\text{CCH}_3)_6(3\text{-Et-Py})_3)$  ( $\text{C}_7\text{H}_8$ ) $^{0.5}$  which exhibits an isosceles  $\text{Fe}_3\text{O}$  triangular plane at room temperature, i.e., completely valence-trapped on the X-ray time scale. However, the analogous mixed-valence  $(\text{Fe}_3\text{O}(\text{O}_2\text{CCH}_3)_6(3\text{-Et-Py})_3)$  ( $\text{CH}_3\text{CCl}_3$ ) shows a valence detrapping phenomenon due to the adoption of a symmetric solvate molecule configuration. Thus, one really can turn on and off the intramolecular electron transfer in the mixed-valence complexes by controlling the lattice environments.

The gold(I) oxo complexes  $[\text{LAu}(\mu_3\text{-O})\text{BF}_4]$  (1) have been prepared for  $\text{L} = \text{PMePh}_2, \text{PMe}_2\text{Ph}, \text{PEtPh}_2, \text{PPriPh}_2, \text{P(p-ClPh)}_3, \text{P(o-tol)}_3, \text{P(OEt)Ph}_2, \text{P(OMe)}_3$  and  $\text{P(mesityl)}_3$ . Two of these new oxo complexes were structurally characterized. The  $\text{PMePh}_2$  structure consists of inversion-related edge-bridged  $[\text{LAu}(\mu_3\text{O})\text{BF}_4]$  units. New gold oxo complexes are also formed in equilibrium mixtures of  $[\text{LAu}(\mu_3\text{-O})\text{BF}_4]$  and  $\text{L}'\text{AuCl}$ . Oxygen-17 NMR data for 1 show chemical shifts of 19.7 to  $-\$36.0$  ppm ( $\text{H}_2\text{O}$  reference) with upfield shifts corresponding to increasing basicity of the phosphine, L. The new oxo complexes may be converted into the analogous imido, hydrazido and hydroxyimido complexes. The synthetic procedure is straightforward. The stability of the hydrazido and hydroxyimido complexes appears to depend upon both the electron density on the diazene nitrogen and steric protection of the phosphine ligand. Among

these, dimethyl hydrazido and hydroxyimido complexes are the first isolated intermediates in the reduction of gold(I) to gold clusters. The cone angle is a major factor in determining the formation of gold clusters.  $[\text{AuL}]_3$  is suggested as a reactive intermediate in the dialkylhydrazido decomposition process. Most interestingly,

$[\text{AuL}]_3\text{NN}(\text{AuL})_3$  (10, 11) are the first dinitrogen complexes with the dinitrogen at the center of six metal atoms, as proposed for the bonding of  $\text{N}_2$  to the  $\text{FeMo}$  nitrogenase cluster. Formal oxygen atom transfer to CO from the oxo complexes  $[\text{LAu}(\mu_3\text{-O})\text{BF}_4]$  is an extremely useful reaction, allowing the preparation of new gold clusters and known gold clusters in dramatically greater yield than those of previous methods. *t*-BuNC is not as mild and selective as CO in the formation of gold clusters. Among the new gold clusters that have been made,  $[\text{Au}_8(\text{P(mesityl)}_3)_6(\text{BF}_4)_3]$  (20) and  $[\text{AuP(mesityl)}_3]_4(\text{BF}_4)_2$  (21) are particularly attractive. 20 is unique for its high Au-to-phosphine ratio and very open structure. 17 represents the smallest possible polyhedral gold clusters. Gold clusters also participate in oxo exchange reactions. The reactions may be formal oxygen atom transfers between clusters. Reduction of  $\text{NO}$  to  $\text{N}_2\text{O}$  is achieved by gold sulfido complex  $[\text{AuPPh}_3]_2\text{S}$ .  $[\text{Au}_2\text{PPh}_3]_2$  is the reaction intermediate, which has been isolated and characterized. Synthesis of gold(I) nonlinear optical compounds are attempted. Complex  $[\text{AuPPh}_3]_6\text{HNC}_6\text{H}_5\text{NO}_2$  is obtained by addition of excess  $\text{HNC}_6\text{H}_5\text{NO}_2$  to either  $\text{PPh}_3\text{Au(acac)}$  or  $\text{PPh}_3\text{AuO}^t\text{Bu}$ . The synthetic route to  $[\text{AuL}]_2\text{NC}_6\text{H}_4\text{NO}_2$  involves treatment Au imido complex  $[\text{AuL}]_3\text{NC}_6\text{H}_4\text{NO}_2$  with  $\text{Cl}^-$  source.

This collection of 24 papers examines the numerous ways in which the stars influenced our ancestors' view of the world. From Stonehenge and Ramesside star clocks to the use of ropes in astronomy, and even an Orion-based pregnancy calendar, this volume covers a vast array of periods and places.

Legacies of Astronomy in Culture : Proceedings of the 9th Annual Meeting of the European Society for Astronomy in Culture (SEAC), The Old Observatory, Stockholm, 27-30 August 2001

A journal of physical sciences. A  
Calendars, Symbols and Orientations  
Regular papers & short notes. Part 1  
Piezoelectric Materials

Our Civic Life SB3 Citizenship in a Democracy  
"The reactive complexes  $\text{CpRu}(\text{PPh}_3)_2\text{SR}$  ( $\text{Cp} = \eta^5\text{-cyclopentadienyl}$ ;  $\text{R} = \text{H}, 4\text{-C}_6\text{H}_4\text{Me}, 1\text{-C}_6\text{H}_7, \text{CHMe}_2$ ) were



prepared by briefly heating  $\text{CpRu}(\text{PPh})_3\text{Cl}$  with LiSR in refluxing THF. Treatment of the thiolates with CO gave  $\text{CpRu}(\text{PPh})_3(\text{CO})\text{SR}$ . The reaction of  $\text{CS}_2$  with  $\text{CpRu}(\text{PPh})_3\text{SR}$  gave the thioxanthate complexes  $\text{CpRu}(\text{PPh})_3(\text{S})_2\text{CSR}$  ( $R = 4\text{-C}_6\text{H}_4\text{Me}$ ,  $1\text{-C}_3\text{H}_7$ ,  $\text{CHMe}_2$ ), wherein the  $\text{CS}_2$  inserted into the Ru-S bond. A study of the kinetics of this reaction and the crystal structure of  $\text{CpRu}(\text{PPh})_3(\text{S})_2\text{CS}(1\text{-C}_3\text{H}_7)$  is also reported. Refluxing a toluene solution of  $\text{CpRu}(\text{PPh})_3\text{SR}$  ( $R = 1\text{-C}_3\text{H}_7$ ,  $\text{CHMe}_2$ ) gave, via sequential loss of  $\text{PPh}$  the dimeric complexes ( $\text{CpRu}(\text{PPh})_3\text{SR}$ ) $_2$  which converted into the complexes ( $\text{CpRuSR}$ ) $_3$ . The crystal structure of ( $\text{CpRuS}(1\text{-C}_3\text{H}_7)$ ) $_3$  is reported. The reaction of  $\text{SO}_2$  with  $\text{CpRu}(\text{PPh})_3\text{SR}$  ( $R = 4\text{-C}_6\text{H}_4\text{Me}$ ,  $1\text{-C}_3\text{H}_7$ ,  $\text{CHMe}_2$ ) gave the complexes  $\text{CpRu}(\text{SO}_2)(\text{PPh})_3\text{S}(\text{SO}_2)\text{R}$ . A reaction mechanism is proposed and the x-ray structure of  $\text{CpRu}(\text{SO}_2)(\text{PPh})_3\text{S}(\text{SO}_2)(4\text{-C}_6\text{H}_4\text{Me})$  was determined. The stable complex  $\text{CpRu}(\text{PPh})_3(\text{CO})\text{S}(\text{SO}_2)(\text{CHMe}_2)$  was observed by  $^1\text{H}$  and IR spectroscopy. The complex  $\text{CpRu}(\text{SO}_2)(\text{PPh})_3\text{S}(4\text{-C}_6\text{H}_4\text{Me})$  was prepared by melting  $\text{CpRu}(\text{SO}_2)(\text{PPh})_3\text{S}(\text{SO}_2)(4\text{-C}_6\text{H}_4\text{Me})$ . The complexes  $\text{CpRu}(\text{PPh})_3(\text{CO})\text{SER}$  ( $E = \text{S}$ ,  $\text{SS}$  and  $\text{S}(\text{O})$ ;  $R = 4\text{-C}_6\text{H}_4\text{Me}$ ,  $1\text{-C}_3\text{H}_7$ ,  $\text{CHMe}_2$ ) were prepared by the reaction of the thiol  $\text{CpRu}(\text{PPh})_3(\text{CO})\text{SH}$  with the appropriate phthalimide sulfur transfer reagents  $\text{REphth}$  ( $\text{phth} = \text{phthalimide}$ ). The x-ray structures of  $\text{CpRu}(\text{PPh})_3(\text{CO})\text{SS}(\text{CHMe}_2)$ ,  $\text{CpRu}(\text{PPh})_3(\text{CO})\text{SSS}(1\text{-C}_3\text{H}_7)$ ,  $\text{CpRu}(\text{PPh})_3(\text{CO})\text{SS}(\text{O})(\text{CHMe}_2)$  and  $\text{CpRu}(\text{PPh})_3(\text{CO})\text{SS}(\text{O})_2(4\text{-C}_6\text{H}_4\text{Me})$  are discussed." --

A number of ectomycorrhizal (ECM) fungi, from sites uncontaminated by toxic metals, were investigated to determine their sensitivity to  $\text{Cd}^{2+}$ ,  $\text{Pb}^{2+}$ ,  $\text{Zn}^{2+}$  and  $\text{Sb}^{3-}$ , measured as an inhibition of fungal biomass production. Isolates were grown in liquid media amended with the metals, individually (over a range of concentrations) and in combination (at single concentrations) to determine any significant interactions between the metals. Significant interspecific variation in sensitivity to  $\text{Cd}^{2+}$  and  $\text{Zn}^{2+}$  was recorded, while  $\text{Pb}^{2+}$  and  $\text{Sb}^{3-}$  individually had little effect. The presence of  $\text{Pb}^{2+}$  and  $\text{Sb}^{3-}$  in the media did however, ameliorate  $\text{Cd}^{2+}$  and  $\text{Zn}^{2+}$  toxicity in some circumstances. Interactions between  $\text{Cd}^{2+}$  and  $\text{Zn}^{2+}$  were investigated further over a range of concentrations.  $\text{Zn}^{2+}$  was found to significantly ameliorate the toxicity of  $\text{Cd}^{2+}$  to three of the four isolates tested. The influence of  $\text{Zn}^{2+}$  varied between ECM species and with the concentrations of metals tested. Transition metal-mediated oxygen, nitrogen, and sulfur transfer reactions to olefins and acetylenes were reviewed in Chapter 1. The alkyl osmium(VI) complexes ( $\text{Y}$ ) ( $\text{Os}(\text{N})(\text{R})_2\text{Cl}$ ),  $\text{Os}(\text{N})(\text{CH}_2\text{SiMe}_3)_2\text{Cl}$ ,  $\text{Os}(\text{N})(\text{CH}_2\text{SiMe}_3)_2\text{Cl}(\text{NC}_5\text{H}_5)$ ,  $\text{Os}(\text{N})(\text{CH}_2\text{SiMe}_3)_3(\text{Z})$  and  $\text{Os}(\text{N})(\text{CH}_2\text{SiMe}_3)_2(\text{X})_2$  ( $\text{BF}_4$ ) where  $\text{Y} = \text{NBu}_4$ ,  $\text{PPh}_4$ ;  $\text{R} = \text{CH}_2\text{SiMe}_3$ ,  $\text{Me}$ ;  $\text{Z} = \text{NC}_5\text{H}_5$ ,  $\text{PMe}_3$ ,  $\text{PPh}_3$ ;  $\text{X} = \text{NC}_5\text{H}_5$ ,  $\text{NCCH}_3$ , were synthesized in Chapter 2. Nitrido and

imido osmium(VI) complexes were prepared and their reaction chemistry was studied in Chapter 3. Improved syntheses of  $(\eta^5\text{-C}_5\text{H}_5)_2\text{Os}(\text{N})(\text{CH}_2\text{SiMe}_3)_2$  and  $(\eta^5\text{-C}_5\text{Me}_5)_2\text{Os}(\text{N})(\text{CH}_2\text{SiMe}_3)_2$  were described, while that of  $(\eta^5\text{-C}_5\text{H}_5)_2\text{Os}(\text{N})\text{Me}$  was newly developed. The corresponding imido complexes were prepared using methyl trifluoromethanesulfonate. The imide,  $(\eta^5\text{-C}_5\text{H}_5)_2\text{Os}(\text{N})(\text{CH}_2\text{SiMe}_3)_2$  ( $\text{OSO}_2\text{CF}_3$ ), was deprotonated with triphenylphosphine, pyridine or water forming  $(\eta^5\text{-C}_5\text{H}_5)_2\text{Os}(\text{N}=\text{CH}_2)(\text{CH}_2\text{SiMe}_3)_2$ . This compound can be reprotonated with strong acids. The reaction of  $(\eta^5\text{-C}_5\text{H}_5)_2\text{Os}(\text{N})(\text{CH}_2\text{SiMe}_3)_2$  ( $\text{OSO}_2\text{CF}_3$ ) with ethylene produced  $(\eta^5\text{-C}_5\text{H}_5)_2\text{Os}(\text{HN}=\text{CH}_2)(\text{CH}_2\text{SiMe}_3)_2$  ( $\text{OSO}_2\text{CF}_3$ ). Under pressures of ethylene,  $(\eta^5\text{-C}_5\text{H}_5)_2\text{Os}(\text{N})(\text{CH}_2\text{SiMe}_3)_2$  ( $\text{OSO}_2\text{CF}_3$ ) yielded a nitrogen-containing organic compound. Oxygen- and sulfur-containing osmium(VI) complexes were prepared in Chapter 4. The  $\mu_3$ -sulfido osmium(VI) cluster ( $\text{NBu}_4$ ) $_4$  ( $(\text{Os}(\text{N})(\text{CH}_2\text{SiMe}_3)_2)_3(\text{S})_2$ ) was synthesized and its x-ray structure was obtained. The sulfido cluster reacts with  $(\text{Cu}(\text{NCCH}_3)_4)(\text{PF}_6)$  and triphenylphosphine to give a copper-sulfur adduct and triphenylphosphine sulfide. The oxo osmium complex  $(\text{Os}(\text{N})(\text{CH}_2\text{SiMe}_3)_2)_4(\text{O})_2$  was synthesized and reacted with triphenylphosphine giving triphenylphosphine oxide. The three complexes  $(\text{Os}(\text{N})(\text{CH}_2\text{SiMe}_3)_2(\text{OH}))_2$ ,  $(\text{NBu}_4)_4$  ( $(\text{Os}(\text{N})(\text{CH}_2\text{SiMe}_3)_3(\text{OH}))$  and  $(\text{NBu}_4)_4$  ( $(\text{Os}(\text{N})(\text{CH}_2\text{SiMe}_3)_2(\text{OH}))_2$ ) were prepared. Nitrido osmium(VI) amino and amido complexes were synthesized in Chapter 5. The amino complexes included  $\text{Os}(\text{N})(\text{CH}_2\text{Si}(\text{CH}_3)_3)_2(\text{NH}_2\text{CH}_3)_2\text{Cl}$ ,  $(\text{Os}(\text{N})(\text{CH}_2\text{Si}(\text{CH}_3)_3)_3)_2(\text{NH}_2\text{CH}_3)_2$  ( $\text{BF}_4$ ),  $(\text{Os}(\text{N})\text{Cl})_2(\text{NH}_2\text{CH}_3)_3$  ( $\text{Cl}$ ),  $\text{Os}(\text{N})(\text{CH}_2\text{SiMe}_3)_3(\text{NH}_2\text{Bu}_t)$  and  $(\text{Os}(\text{N})(\text{CH}_2\text{Si}(\text{CH}_3)_3)_2)_2(\text{NC}_5\text{H}_5)(\text{NH}_2\text{Bu}_t)$  ( $\text{BF}_4$ ), while the amido compounds included  $(\text{NBu}_4)_4$  ( $\text{Os}(\text{N})\text{Cl}_3(\text{NH}_2\text{Bu}_t)$ ) and  $(\text{NBu}_4)_4$  ( $\text{Os}(\text{N})(\text{CH}_2\text{SiMe}_3)_2\text{Cl}(\text{NH}_2\text{Bu}_t)$ ).

Japanese Journal of Applied Physics  
 Proceedings of the 7th International Conference  
 'Bituminous Mixtures and Pavements' (7ICONFBMP),  
 June 12-14, 2019, Thessaloniki, Greece  
 Logic Optimization  
 Synthesis of Finite State Machines  
 Giving the Best Phonographic Forms for the Words of the  
 English Language  
 Workplan. Part A. Part B : Field sampling plan ; remedial  
 investigation/feasibility study, Load-Assemble-Package  
 (LAP) Area, Joliet Army Ammunition Plant, Joliet, Illinois  
 The purpose of this study was to document the  
 rheological measurements made for Sludge Batch 3  
 (SB3) and the blend of SB3 with Sludge Batch 2  
 (SB2). These measurements were primarily made on  
 Slurry Mix Evaporator (SME) products, i.e. melter  
 feeds. Some measurements were made on SB2/3  
 blend Sludge Receipt and Adjustment Tank (SRAT)

products. Measurements on radioactive SB3 and SB2/3 samples have been limited to sludge characterization. SB2/3 measurements studied the impact of changing the SRAT acid addition strategy on the SRAT and SME product rheology. SB2/3 measurements also studied the impact of changing the waste loading target (sludge oxides content in glass) of the SME product. SB3 measurements studied the impact of changes in the wash end point and acid addition strategy on the SME product (melter feed) rheology. A summary of the significant findings is given below: SB3 radioactive sludge and blended SB2/3 radioactive sludge were less viscous than SB2 radioactive sludge. SB2/3 blend sludge is more viscous than SB3 sludge. SB3 simulant SME product rheology was strongly impacted by changing the noble metal concentrations to more closely match those of the qualification sample. This reduction in noble metals produced a lower pH product that was also considerably less viscous. Increased acid addition in the SB2/3 SRAT generally led to less viscous simulant SRAT products. This trend did not persist in the SME products. SME products became more viscous when increased acid was used in the SRAT cycle from 135 per cent up to 170 per cent of stoichiometry, then became less viscous as total acid was increased further to 185 per cent. A significant increase in hydrogen generation occurred between 170 per cent and 185 per cent. The impact of acid addition on SB3 SME products was also variable. The impact of waste loading changes from 31 to 35 to 40 per cent on SB2/3 simulant SME products led to more viscous melter feeds as waste loading increased at constant wt. per cent total solids. The slurry pH seemed to be having a significant effect on the rheological variations within a set of similar simulant samples. The most viscous slurry in a set often had an intermediate pH in the 5-8 range. Rheological differences were seen as a function of wash endpoint with simulants. The Case 7d SB2/3SME product was more viscous than the less-washed Case 6b SME product. The more-washed SB3 simulant SME products that started at 20,000 mg/kg sludge nitrite were more viscous than the less washed SB3 simulant SME products that started at 27,000 mg/kg sludge nitrite.

This synthesis of post-fire treatment effectiveness reviews the past decade of research, monitoring, and product development related to post-fire hillslope emergency stabilization treatments, including erosion barriers, mulching, chemical soil treatments, and combinations of these treatments. In the past ten years, erosion barrier treatments (contour-felled logs and straw wattles) have declined in use and are now rarely applied as a post-fire hillslope treatment. In contrast, dry mulch treatments (agricultural straw, wood strands, wood shreds, etc.) have quickly gained acceptance as effective, though somewhat expensive, post-fire hillslope stabilization treatments and are frequently recommended when values-at-risk warrant protection. This change has been motivated by research that shows the proportion of exposed mineral soil (or conversely, the proportion of ground

cover) to be the primary treatment factor controlling post-fire hillslope erosion. Erosion barrier treatments provide little ground cover and have been shown to be less effective than mulch, especially during short-duration, high intensity rainfall events. In addition, innovative options for producing and applying mulch materials have adapted these materials for use on large burned areas that are inaccessible by road. Although longer-term studies on mulch treatment effectiveness are on-going, early results and short-term studies have shown that dry mulches can be highly effective in reducing post-fire runoff and erosion. Hydromulches have been used after some fires, but they have been less effective than dry mulches in stabilizing burned hillslopes and generally decompose or degrade within a year.

The book provides an in-depth discussion regarding inorganic ion exchangers for students, teachers, and researchers engaged in conducting research in chemical technology and related areas. Analytical chemists seeking simple and novel means of using easy-to-prepare chromatographic materials will find this book extremely informative. Inorganic Ion Exchangers in Chemical Analysis is unique in its discussion of column and planar chromatographic applications of amorphous synthetic inorganic ion exchangers. The book also covers the historical background of inorganic ion exchangers, their classification and present status, and the analytical aspects of these materials.

Munson's System of Phonography

The Messenger of Mathematics

A Summary of Rheology Data For SB3 and SB2